Rain Energy Harvesting Using Atomically Thin Gadolinium Telluride Decorated 3D Printed Nanogenerator

Partha Kumbhakar, Arko Parui, Rushikesh S. Ambekar, Madhubanti Mukherjee, Saif Siddique, Nicola M. Pugno, Abhishek K. Singh, and Chandra S. Tiwary*

The 3D printing (3DP) technology offers an innovative approach to developing energy storage devices to create facile and low-cost customized electrodes for modern electronics. Generating electric potential by moving a droplet of ionic solution over 2D materials is a novel method for rain energy harvesting. This work demonstrates a liquid-solid contact electrification-based 3DP nanogenerator where raindrop passes through the positively charged ultrathin gadolinium telluride (Gd_2Te_3) sheets. The output efficiency of the nanogenerator is increased to ≈400% by enhancing the surface area of copious 3D-printed porous structures. The density functional theory (DFT) calculations reveal that the high electrical conductivity of (112) surface of Gd_2Te_3 is due to the p-type charge carriers, which help to generate electricity by interacting with the ionic solution. This work can open up a new avenue to advance scientific research on blue energy harvesting and tackle the energy crisis.

1. Introduction

The limited availability of fossil fuels and their negative environmental impacts have driven the research for sustainable technologies to meet current energy challenges. Hydropower-based energy seems to be the only contender to replace traditional energy generation systems among the existing technologies. With the abundance of water on the earth's crust, generating electricity from flowing water is still an enticing opportunity. If we consider the example of rainfall, an enormous amount of energy can be harvested from it if the energy of each drop is successfully converted to electrical output and stored.[1–4] Each raindrop carries energy in two forms: the kinetic energy when they fall and the electrostatic energy due to friction with other water droplets or air molecules,[5] New and effective technology is required to convert and store this energy efficiently. Researchers have made smart materials capable of converting the kinetic energy of liquid into electricity.[6–8] There are two techniques for inducing local drop motion: a) direct contact and b) contactless technique. Contactless methods have several advantages, such as loss of liquid mass, surface contamination, and manipulation of the desired precision of the liquid drop. They involve electrowetting, dielectrophoresis, and charge printing.[9,10] Innovative techniques such as using magnetic field variations and light-induced capillary forces to tubular microactuators to propel liquid have also been suggested.[11] Printing-based technologies for self-powered devices are studied, such as direct-write printing of Ag electrodes, contact printing of liquid metal, and the screen-printing of carbon nanotubes. Such conductive ink can be utilized as a template for energy harvesting. Recently, 3D printing-based flexible, efficient, and economical energy storage devices have gained huge popularity[12–15] due to their several advantages such as flexibility, geometry controllability, lightweight, customizable, high mechanical property, single printing system for complex or different materials, etc.[16–18] Since the amount of energy generation directly depends on contact surface area, 3D printing can be a crucial technique as it can easily be utilized to fabricate complex porous structures that can provide a higher surface area.[19–24] Building 3D printed systems of atomically thin 2D materials of high surface area with unique physical and chemical properties opens up a new advancement for making flexible electrode materials.

Recently, promising new 2D materials gained remarkable attention due to their distinctive properties, such as extraordinary flexibility and high functionalization ability with different surfaces (metal, polymer, ceramics).[25] These properties are

P. Kumbhakar, R. S. Ambekar, S. Siddique, C. S. Tiwary
Department of Metallurgical and Materials Engineering
Indian Institute of Technology Kharagpur
West Bengal 721302, India
E-mail: chandra.tiwary@metal.iitkgp.ac.in

A. Parui, M. Mukherjee, A. K. Singh
Materials Research Centre
Indian Institute of Science
Bangalore 560012, India

N. M. Pugno
Laboratory of Bio-inspired
Bionic
Nano
Meta Materials and Mechanics
Department of Civil, Environmental and Mechanical Engineering
University of Trento
Calepina, 14 - 38122 Trento, Italy

N. M. Pugno
School of Engineering and Materials Science
Queen Mary University of London
Mile End Road, London E1 4NS, UK

The ORCID identification number(s) for the author(s) of this article can be found under https://doi.org/10.1002/adsu.202200296.

mostly thickness and layer-dependent. 2D materials interact with the surrounding surface with a van der Waals interaction. The adhesive property between the layers of 2D materials and external surfaces may be increased by the presence of chemical bonding/interaction. Therefore, these advantageous properties of 2D materials improve the energy generation from the movement of droplets. Among other 2D materials, 2D Tellurides have attracted much attention in the past few decades due to their topological semimetal nature, magnetic properties, and superconducting behavior.[26,27] When rare earth metals are alloyed with tellurides, they add new dimensions to the already rich physical and chemical properties of tellurides [28–30] The large surface area offered by 2D material makes it a promising material for drop motion studies.[8] Additionally, only the top layer, in contact with the liquid, generates voltage; the other layers act as shunt resistors dividing the output voltage when the system is considered a nanogenerator circuit. Therefore, the lesser the number of layers more excellent the output voltage.[31] The structure of the Gd-Te system has two sites for Gd and three for Te; it does not have any cation vacancies or sites for other atoms.[32,33] Because of its similarity with tetradymite structures (A_2X_3; A = Bi, Sb, and X = Se, Te), Gd-chalcogenides show the best thermoelectric properties among all the rare-earth chalcogenides, with Gd_2Te_3, in particular, having a power factor of $0.6 \times 10–6$ W K^{-1} cm^{-1}.[33] The material exhibited semi-metallic behavior and an antiferromagnetic magnetic ground state.

The present work reports the yet unexplored physical properties of 2D Gd_2Te_3 as energy harvesting materials. The ultrathin Gd_2Te_3 decorated 3D-printed structures act as a flexible device for energy harvesting by manipulating drops of ionic liquid on its active surface, as shown in **Figure 1**. The decorated 3D-printed structure enhances the overall performance by contact electrification and raindrops impulse. Different types of 3D-printed porous structures are employed to study the effect of porosity and effective surface area in energy generation.

Detailed density functional theory (DFT) calculations were also performed to gain insight into the origin of voltage generation by Gd_2Te_3 coated 3D printed structure and the nature of the charge carrier. This work has the potential to make a significant impact on the generation of an accessible and sustainable energy system for the growth of sustainable cities and communities. We think that by doing this effort, we can take a small step toward realizing the sustainable development aim.

2. Results and Discussion

2.1. Characterization of Atomically-Thin Gd_2Te_3

Figure 2A shows the X-ray diffraction (XRD) pattern of bulk Gd_2Te_3. The pattern matches the *Pnma* phase with an Sb_2S_3 (stibnite) structure. Figure 2B (upper panel) shows the digital photograph of the bulk Gd_2Te_3 crystal with a size of a few centimeters. These crystals were extremely brittle and showed a planar fracture surface as observed by scanning electron microscopy (SEM) (Figure S1, Supporting Information). Composition analysis was performed using energy-dispersive X-ray spectroscopy (EDX) to ensure that proper composition had been achieved (Figure S2, Supporting Information). The results for the selected area show that the sample has 56.56% of Te and 43.44% Gd by mass. Gd_2Te_3 is made up of planar sheets stacked on top of one another, making it a layered crystal. Ultrathin layers of Gd_2Te_3 samples were synthesized from these bulk crystalline solids, which were powdered initially and then exfoliated with an organic solvent, isopropyl alcohol (IPA) (more details, see Experimental Section). This enables us to obtain a dispersion of 2D sheets by adding Gd_2Te_3 powder in IPA and agitating the mixture using a probe-sonicator for 30 min at room temperature. The vibrational energy provides energy to overcome the van der Waals forces binding
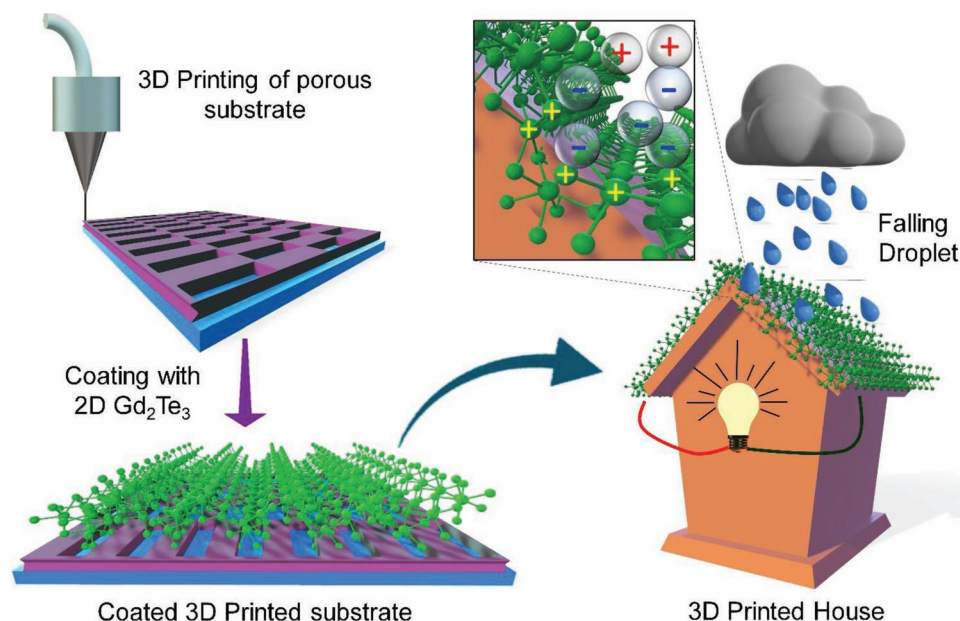

Figure 1. Schematic representation of fabrication of 3D printed devices decorated with ultrathin Gd_2Te_3 and energy generation using liquid droplets.
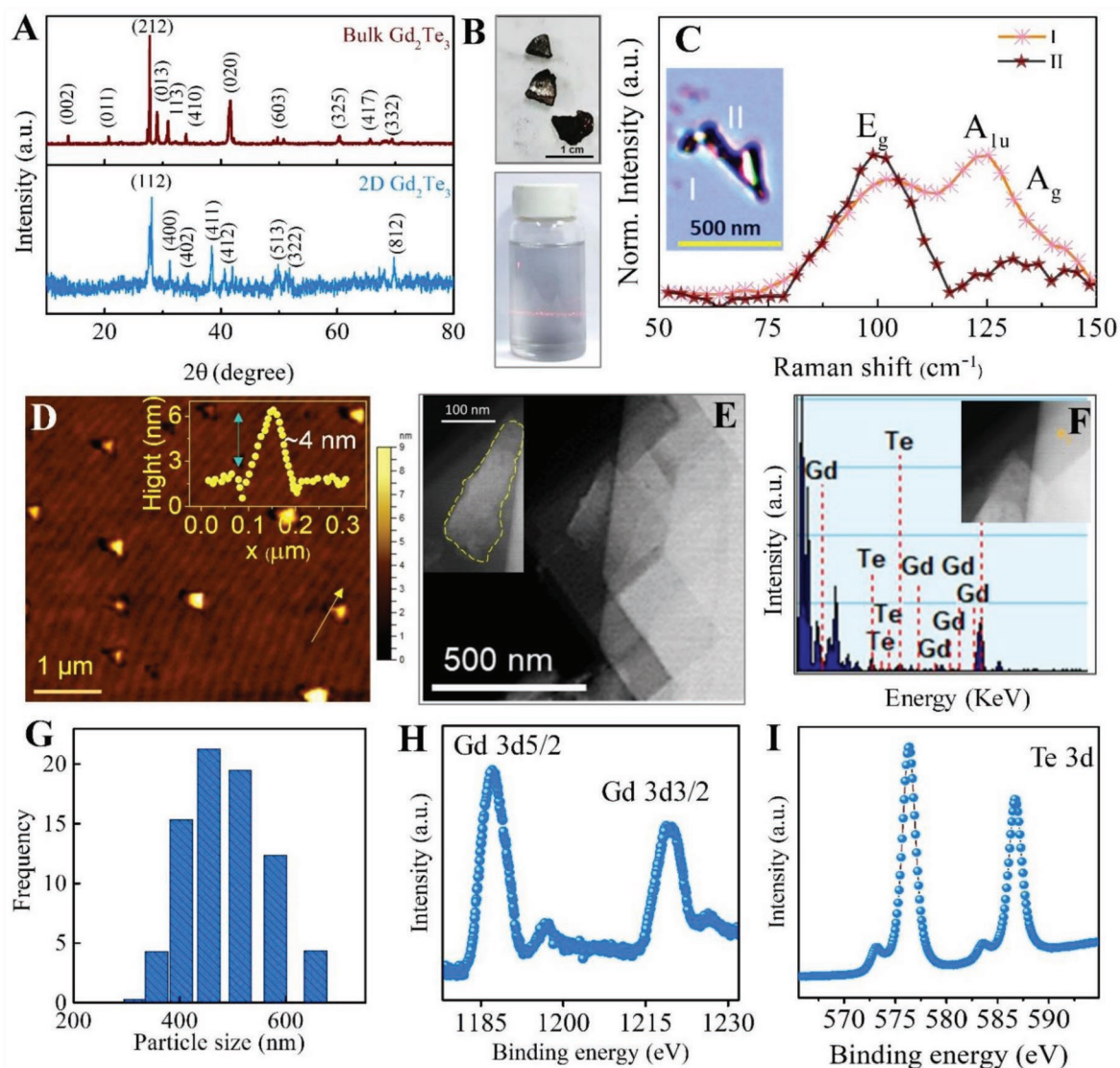
**ADVANCED
SCIENCE NEWS**

www.advancedsciencenews.com

**ADVANCED
SUSTAINABLE
SYSTEMS**

www.advsustainsys.com

Figure 2. Structural characterizations of exfoliated Gd_2Te_3. A) XRD pattern of bulk Gd_2Te_3 and 2D Gd_2Te_3. B) Shows the digital photo of as-synthesized bulk Gd_2Te_3 and the dispersion of 2D Gd_2Te_3 in IPA after liquid exfoliation. C) Raman spectra of 2D Gd_2Te_3 of varying thickness and D) AFM and line profile of 2D Gd_2Te_3 drop-casted on a Si substrate. E) Bright-field TEM image of the exfoliated sheets, inset shows a single nanosheet of Gd_2Te_3. F) An EDX spectrum showing Gd and Te. G) Average particle size analysis of exfoliated samples. The XPS spectrum of the 2D Gd_2Te_3 with fitted peaks for H) Gd 3d and I) Te 3d.

the layers and separating them. The XRD was carried out on 2D Gd_2Te_3 with Cu-Kα radiation ($\lambda = 1.54$ Å) in the 2θ range of 10–90° (Figure 2A). The pattern matches with reported literature and the lattice parameters of $a = 11.96$ Å, $b = 4.29$ Å, $c = 11.75$ Å, $\alpha = \beta = \gamma = 90°$ ([33]). The stibnite structure gives the telluride parallel ribbons of $(Gd_4Te_6)_n$ stacked together by weak van der Waals forces, perpendicular to the b-axis.[34] The ribbons are made up of Gd-Te-Gd chains, with Te atoms bonded together at 120°, forming a honeycomb-like structure similar to that of graphene. The digital photograph of exfoliated dispersion of Gd_2Te_3 at room temperature confirms the formation of ultrathin sheets (lower panel of Figure 2B). Additionally, it can be observed that the XRD peaks of 2D Gd_2Te_3 are broader than bulk due to nanostructuring. Also, the overlapping of peaks makes it challenging to distinguish them, and it seems that the

number of observed peaks has decreased.[35] The normalized Raman spectra (λex = 532 nm) and microscopy images of 2D Gd_2Te_3 of varying thickness are shown in Figure 2C and its inset. The distinct Raman peaks were observed at 100 and 125 cm^{-1}. All the spectra had the same peak at 100 cm^{-1}. The A_g ($\approx$125 cm^{-1}) lattice vibration mode strongly depends on layer thickness. The significant difference observed was the emergence of a peak at 125 cm^{-1} as the thickness of the nanosheets varied.[36] For thinner sheets, 125 cm^{-1} Raman mode is more intense. However, it reduces with increasing thickness. The origin of these modes is still unclear, and further investigation is needed. Atomic force microscopy (AFM) results of the exfoliated Gd_2Te_3 show clear triangular sheet-like structures with a height profile of $\approx$4 nm, corresponding to $\approx$3–4 monolayers (Figure 2D). Transmission electron microscopy

**ADVANCED
SCIENCE NEWS**

www.advancedsciencenews.com

**ADVANCED
SUSTAINABLE
SYSTEMS**

www.advsustainsys.com

(TEM) was employed to gain insights into the morphology of the exfoliated 2D sheets. In Figure 2E, we present the bright-field TEM image of the exfoliated sample. The images depict atomically thin triangular sheets agreeing with the triangular units found with AFM results (Inset of Figure 2E). The EDX result confirms the consistency of the atomic ratio of Gd and Te after exfoliation (Figure 2F). The dispersion of exfoliated samples was also analyzed in a particle analyzer, and the average particle size obtained was around 450–500 nm (Figure 2G). Thus, the exfoliation results in sufficiently large sheets with thickness in the order of a few layers. We have performed X-ray photoelectron spectroscopy (XPS) measurements to get more information about the oxidation states and chemical composition of the exfoliated sample (Figure S3, Supporting Information and Figure 2H,I). The XPS analysis shows that the oxidation state of Gd and Te are well-matched with the previous report with proper atomic ratio.

To study the performance of electricity generation from ultrathin Gd_2Te_3 using liquid drop motion, we have fabricated a Gd_2Te_3-based nanogenerator on a 3D-printed porous struc-ture. For the fabrication of the nanogenerator (Figure 1 and see Experimental Section for more details), a thin layer of 2D Gd_2Te_3, mixed with a PVDF binder in a 10:1 ratio, was coated on a 3D-printed porous surface. Following this, the nano-generator was dried on a hot plate for 2 h at 50 °C. Copper metal contacts were placed on the positive and negative elec-trodes at each end of the material. The digital photograph of the 3D-printed coated device is presented in Figure S4A, Sup-porting Information. The static contact angle between the solution drop and 3D printed coting system was measured, and it was found to be ≈95.4 ± 3.8 (Figure S4B, Supporting Information). However, as the droplet moves downwards on the surface of the cell, the shape of the droplet changes. In **Figure 3**A,C, we present the optical microscopy and SEM images of the surface of the 3D printed structure before and after the decorating materials. Triangular sheets are well deco-rated on the polymer substrate. The SEM image, elemental mapping, and EDX spectra also confirm the uniform distribu-tion of the sheets on a 3D-printed object (Figure S5, Supporting Information). The digital photograph of the flexible 3D printed
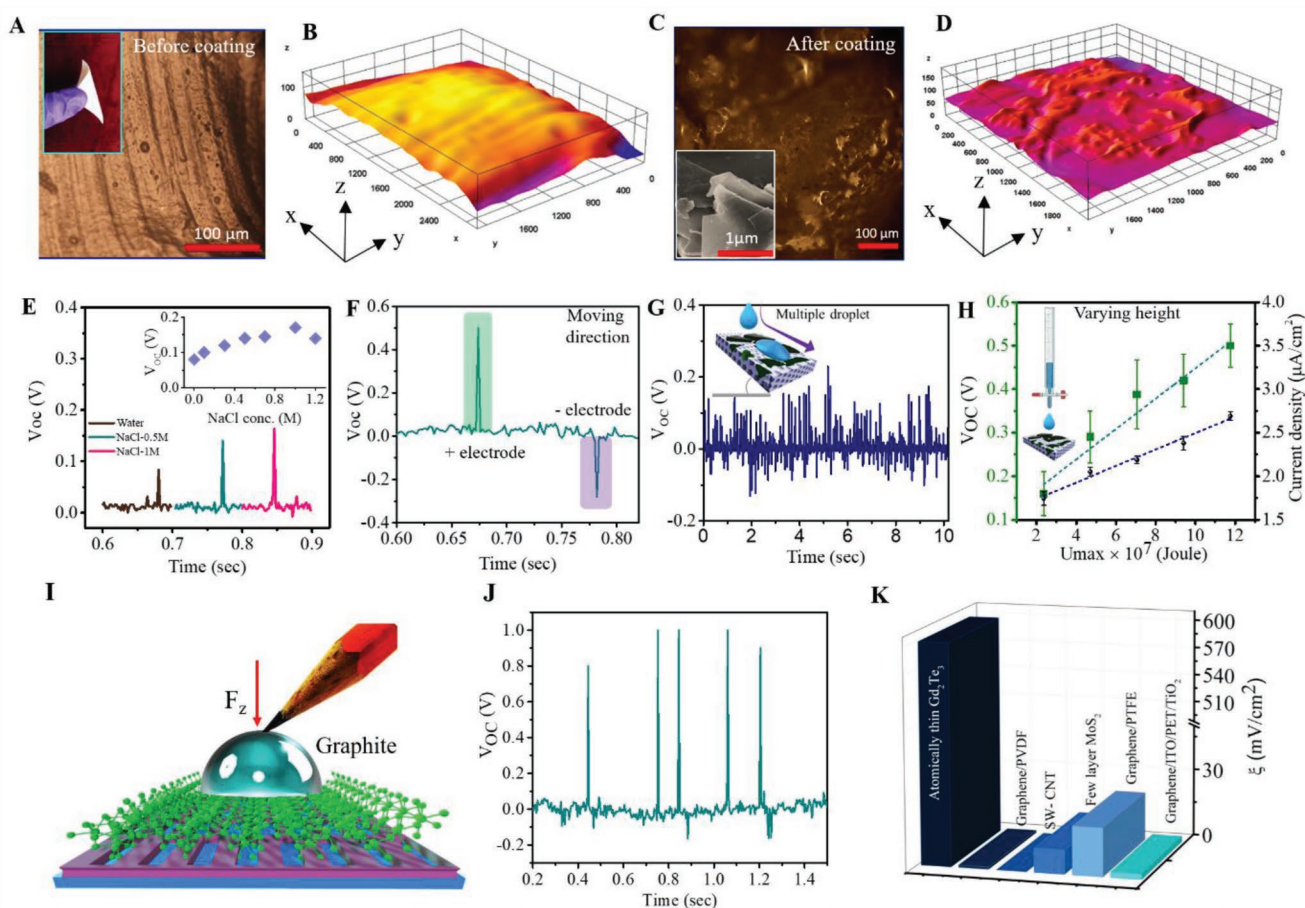

Figure 3. Energy harvesting from droplets. Optical microscopy image and SEM image of 3D printed substrate A) before and C) after decoration with 2D material. The inset of (A) shows the digital photograph of the flexible substrate. 3D surface analysis of the printed structure B) before and D) after decoration. E) Droplets of different ionic concentrations dropped from the same height. The inset shows the output voltage for different concentrations of solution. F) The pulse is generated along the moving direction of the droplet. G) Multiple droplets are generating output voltage. The inset shows the schematic of the measurement setup. H) Output voltage and current density increase versus potential energy at the surface by falling droplets from varying heights. I) Schematic representation of NaCl droplet on cell and moving direction, graphite charge layer. J) The output voltage of the 3D printed cell. K) Comparisons of the liquid droplet-based energy generation with other 2D materials.

**ADVANCED
SCIENCE NEWS**

www.advancedsciencenews.com

**ADVANCED
SUSTAINABLE
SYSTEMS**

www.advsustainsys.com

device is depicted in the inset of Figure 3A. We also presented the 3D surface plot of the substrates, as shown in Figure 3B,D. The surface analysis indicates that after coating with thin sheets, the surface of PLA polymer becomes rough. This will increase the efficacy in the contact time and the effective surface area between droplets and materials.

2.2. Electricity Generation from Gd$_2$Te$_3$ Decorated 3D Printed Surface

Solid–liquid contact electrification of the 2D Gd$_2$Te$_3$ material was tested with different sodium chloride (NaCl) solution concentrations. The output voltage was observed at the end of each electrode connected to a digital oscilloscope. For a standard test, the optimized experimental parameters are the volume of NaCl droplet is ≈20 µL falling from a distance of 6 cm on the 3D printed nanogenerator, which is inclined at an angle of ≈15°. The induced output voltage strongly depends on the concentration of the ions present in the droplets. To measure the dependence of output voltage on the ion concentration of brine solution, pure DI water and different concentration of NaCl solutions (ranging from 0.1 to 1.2 M NaCl) were allowed to flow on the nanogenerator in a static position. The compared voltages are shown in Figure 3E. Interestingly, there is an increase in the voltage response as NaCl concentration in water increases and saturates after 1 M. The low concentration of the salt solution can support the ion transfer process which increases the charge transferred at the solid–liquid interface, thus resulting in a large electrical output. However, as the concentration of the salt solution further increases, more ions will be adsorbed on the device surface and hinder the charge transfer process.[37] A voltage response for the movement of the liquid droplet on the triangular 2D Gd$_2$Te$_3$ was measured (Figure 3F). The output voltage shows a sharp response to the movement direction of the droplet. When the droplet moves at a constant velocity on the device, an output voltage of around ≈0.5 V was generated in a different direction, that is, the positive and negative electrodes of the device. This leads to a charge redistribution in the droplet generating electric signals that pass through the external circuit. The output voltage fluctuation is due to the non-uniform distribution of the triangular 2D Gd$_2$Te$_3$ with the 3D-printed substrate.

To test the feasibility of an as-developed setup as an energy harvesting device, multiple droplets of 1M NaCl solution were moved onto a ≈15° tilted cell dropped from a height of 6 cm. Output voltages in the range of ≈0.4 to ≈0.6 V were recorded (Figure 3G and Movie S1, Supporting Information). We can thus see that the setup works perfectly for a continuous flow of droplets without losing any efficiency. The inset of Figure 3G shows a schematic representation of multiple droplet movement directions on the decorated 3D-printed cell. The layers of 2D Gd$_2$Te$_3$ are distinctively shown to represent the charge interaction between the layers. To assess the effect of sliding angles on the output voltage, we measured output voltage by inclining the nanogenerator at different angles. We start from 5° of inclination, and as we reach 15°, we get the maximum voltage. This indicates that the output voltage linearly increases with the increasing velocity of the ionic drop. As

the sliding angle increases, the contact angle also increases (Figures S6 and S7, Supporting Information), covering a larger surface area and producing more output voltage. The decorated 3D-printed device is inclined at an angle of ≈15°, giving the droplet a smaller pace of movement. Because a larger surface is being covered, more charges interact on the material junction and drop, generating a larger voltage. We also studied the effect of the dripping height of droplets in voltage generation (Figure 3H). We calculate the potential energy (U_{max}) by falling droplets on the coated substrate. A linear increase in the output voltage up to ≈0.5 V in the range of 2.35 to 11. 76 × 10^{-7} Jule. The result (linear slope, m = 0.034) indicates that the output performance of the device greatly influenced the dripping height of droplets. We have measured the current density for the 3D printed device as a function of dripping height for multiple droplets (Figure 3H). A linear increment of current density was also observed here. We have also calculated the output power density of the device, and it is found to be ≈1.34 µW cm^{-2} for a maximum dripping height of the droplet. Therefore, these decorated 3D printing substrates can be utilized to power up several electronic gazettes. The inset of Figure 3H shows a pictorial representation of the droplet height impacted on the surface, and the cell was inclined at an optimal inclination angle of 15°.

We further advanced the application of a 2D Gd$_2$Te$_3$ decorated 3D printed nanogenerator for energy harvesting by utilizing the dynamics of the ionic solution by applying a graphite rod. We used pencil graphite as conducting substrate. First, we rubbed the graphite and then applied it to the experiment. An increase in the output voltage of the 2D Gd$_2$Te$_3$ surface with NaCl droplet was observed when a layer of graphite was bought near the surface (Figure 3I,J). As the graphite surface touches the NaCl solution, an output voltage is induced repeatedly (Figure 3J). It enhanced the overall performance of the cell and showed an increased output voltage of ≈0.8 V for multiple droplet movement on the cell. The possible mechanism of the generation of output voltage on Gd$_2$Te$_3$ surfaces is discussed schematically in Figure 3I. During the experiment, more surface charges are obtained on the droplet due to the contact of the graphite rod and Gd$_2$Te$_3$ substrate. Graphite with multiple graphene layers is supposedly producing electrostatic charges, which are responsible for the enhanced charge production in the 2D Gd$_2$Te$_3$ cell, as discussed later. In Figure 3K, we have compared the generation of output voltage per unit area (ξ) for other 2D materials. It shows that atomically thin Gd$_2$Te$_3$ decorated 3D printed device shows enhanced performance as compared to other 2D materials.[38–42]

2.3. Optimization of the 3D Printed Surface

The generation of charge due to the contact electrification can be calculated using the formula,[3] $Q = 2eN_AclA$, where e is the primary charge, N_A is the Avogadro constant, c is the concentration of ions in deionized water/solution, l is the thickness of the ion diffusion, and A is the contact area between droplet and Gd$_2$Te$_3$. Therefore, the charge generation strongly depends on the effective contact surface area. To study the effect of contact-specific surface area between
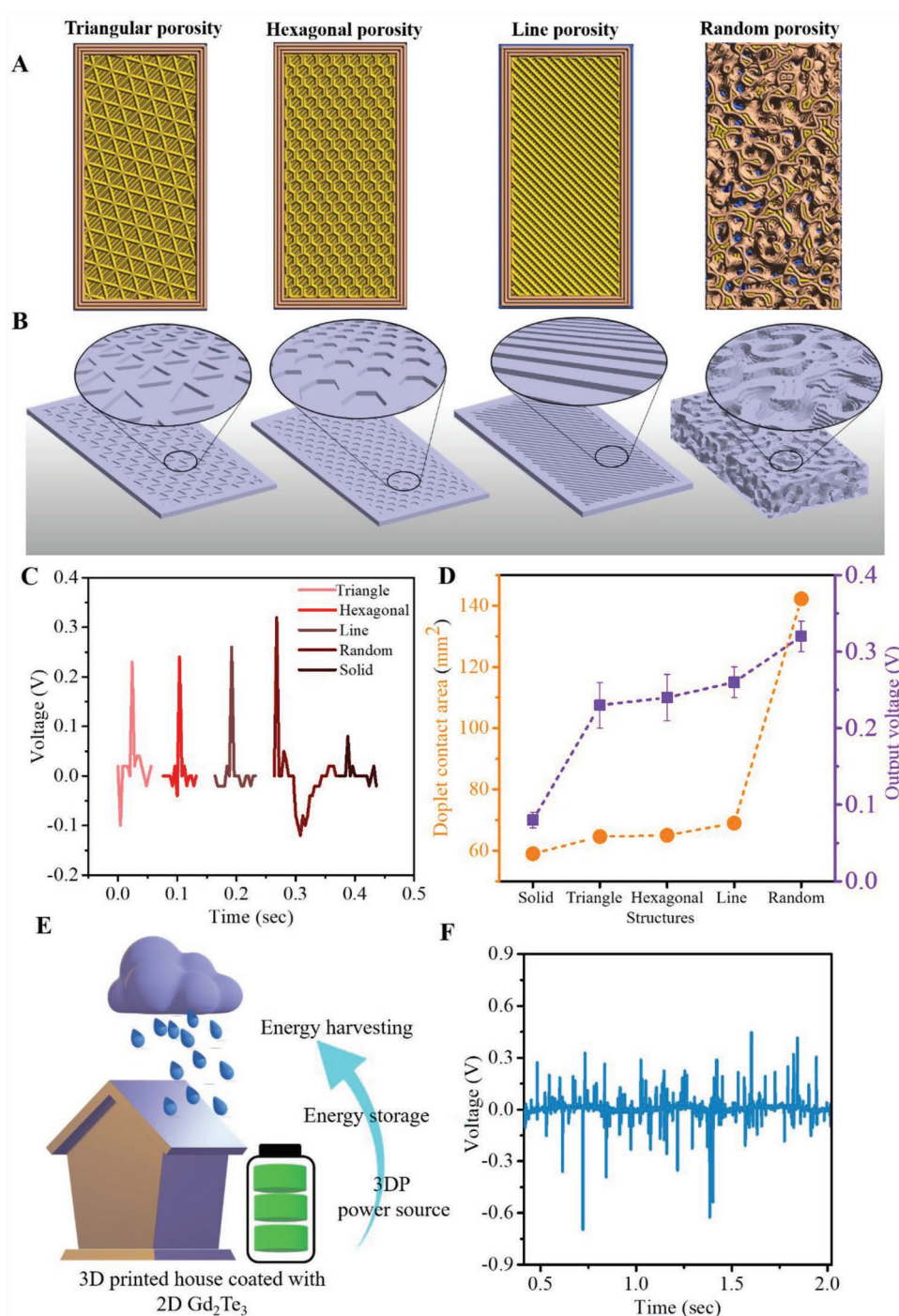
**ADVANCED
SCIENCE NEWS**

www.advancedsciencenews.com

**ADVANCED
SUSTAINABLE
SYSTEMS**

www.advsustainsys.com

Figure 4. Effect of 3D printed architecture on Energy harvesting. A) Top view and B) isometric view of 3D printed porous structures (insect show zoomed region of pores). C) Effect of copious porosity on the output voltage. D) Effect of water droplet contact area on the output voltage. E) 3D printed smart house for energy harvesting from raindrops. F) Output voltage generated from artificial raindrops from 3DP-house.

the droplets and 3D printed structure, a series of 3D-printed structures with different geometry were printed, such as hexagonal, linear, triangular, and structures with random porosity having surface porosity of 33.09%, 39.62%, 16.53%, and 68.71%, respectively. The top and isometric views of these 3D-printed structures are illustrated in **Figures** 4A,B, respectively. To investigate the impact of the geometrical property

of 3D-printed objects, 2D Gd_2Te_3 were uniformly coated on them using a similar coating method. Other parameters such as droplet size, solution concentration, dropping speed, and substrate temperature are fixed to compare the output voltage. The specific contact area increases with the complexity of the 3D printed structures. We have enhanced the surface area of the structures using 3D printing. All the 3D printed

**ADVANCED
SCIENCE NEWS**

www.advancedsciencenews.com

**ADVANCED
SUSTAINABLE
SYSTEMS**

www.advsustainsys.com

structures have greater surface area than the solid surface due to geometrical porosity and surface roughness. 3D printed PLA surface has a higher surface roughness ($R_q = 1.2$ nm) than solid glass ($R_q = 0.39$ nm) surface. The glass surface has lower resilience than the 3D printed polymer surface; therefore, the interaction time of the 3D-printed structure with the droplet is more than the glass surface. In Figure 4C, we demonstrate the output voltage generated by the NaCl droplet. It shows that output voltage increases and gives the highest output for random porosity structures. The output voltage of the random porous structure (≈ 0.32 V) gets enhanced by $\approx 400\%$ compared to the solid structure (≈ 0.08 V) owing to random porosity (≈ 143 mm^2) having a higher surface area than the solid structure (≈ 59 mm^2). The single droplet of 5 mm diameter has ≈ 59 mm^2 surface area; therefore, we have normalized the surface area of all the printed structures by a single droplet contact area. As shown in Figure 4D, the specific contact area is increased with an increase in the complexity of the 3D printed structures. These results can be explained as the surface complexity increases, the porosity also changes, leading to the enhancement of output voltage. However, in the case of a flat solid substrate, the output voltage generation is very low compared to the other structures. Moreover, the high random porosity, more interaction time, and complex contact surface area of 3D printed structures allow us to generate electricity with increased flexibility by tuning the micro-architecture of the structures. Hence higher surface area and interaction time lead to the enhancement of output voltage. More contact time provides more interaction of the ionic solution to the 2D material.

2.4. 3D Printed Energy-Harvesting House: A Proof-of-Concept

To demonstrate the real-life application of droplet-based energy generation from 3D-printed devices, a self-powered 3D printed (3DP) house is designed. It shows the energy harvesting ability from rainwater as schematically presented in Figure 4E. The concentration of the ions in rainwater depends on various aspects, such as geographical regions. The salt concentration will be different in different places. As we observe that the output performance of the device depends on the ionic concentration. Thus, our 3D-printed devices can harvest energy from raindrops in different geographical regions. In general, raindrops contain various ions (Cl$^-$, Na$^+$, K$^+$, Ca$^+$, SO$_4^-$), and the concentration varies with the season. Here, we have chosen NaCl solution as artificial rainwater for demonstration. The ultrathin Gd$_2$Te$_3$ was coated on the 3D-printed floor's roof (Figure S8, Supporting Information). The output voltage is observed under continuous dripping of artificial rainwater (Figure 4F, Figure S8 and Movie S2, Supporting Information). Here, the self-powered 3DP house is an immediate application of energy harvesting from natural resources. To use the 3DP house as a smart house for long-term use, we have tested its stability for 30 days. It is observed that the output voltage is almost the same (Figure S8E, Supporting Information), and the result confirms that the coated 3DP house can be used in energy harvesting under normal environmental conditions.

2.5. Understanding of Electricity Generation from Atomically-Thin Gd$_2$Te$_3$

To get further insight into the voltage generation on the Gd$_2$Te$_3$ surface, we measured the zeta potential (average zeta value $\approx +4.8$ mV) for ultrathin 2D Gd$_2$Te$_3$ in IPA dispersion. The zeta potential (ξ) depends on the electronic charge distribution of the surface and is crucial in controlling the charge adsorption of the materials. Here, we measured the effective surface charge density (σ) to be ≈ 33.37 C m^{-2} from zeta potential using the equation as given below,[43]

$$\sigma = \sqrt{8cN\varepsilon_o\varepsilon_r k_B T}\, \sinh\left(\frac{e\xi}{2k_B T}\right) \tag{1}$$

where c is the ion concentration of the solution, N is the Avogadro constant, k_B is Boltzmann's constant, and T is the temperature, respectively. Further, to get insight into the polarity of the generated surface charge density, we performed first-principles calculations. The bulk Gd$_2$Te$_3$ structure was taken from the Materials Project Database.[44] The optimized lattice parameters for Gd$_2$Te$_3$ were found to be $a = 12.47$ Å, $b = 4.83$ Å, $c = 12.40$ Å has a band gap of 0.77 eV (Figure S9, Supporting Information). Next, three layers of the Gd$_2$Te$_3$ (112) plane made by using the ASE package were chosen for further calculation since it has the most prominent peak in the experimental XRD plot (**Figure 5**A). Lattice parameters of (112) surface were $a = 13.25$ Å, $b = 15.30$ Å, $c = 26.80$ Å. The bandgap of the Gd$_2$Te$_3$ surface is 0.67 eV (Figure S9, Supporting Information) with a work function of 3.74 eV. To understand the charge distribution, we did a Bader charge analysis of the (112) surface, which shows that Te atoms have a negative Bader charge, thereby accepting electrons from Gd atoms having a positive Bader charge. Hence, the considered surface accumulates both negative and positive polarities. However, the concentration of the charges is not the same on the surface. In order to understand the predominating polarity present on the surface, we have calculated the charge accumulation to visualize the charge redistribution on a surface:

$$\Delta\rho = \rho(Gd_2Te_3) - \rho(Gd_2) - \rho(Te_3) \tag{2}$$

where $\rho(Gd_2Te_3)$, $\rho(Gd_2)$, and $\rho(Te_3)$ are the charge densities of an isolated system of Gd$_2$Te$_3$, Gd$_2$, and Te$_3$, respectively. The charge accumulation-depletion plot (Figure 5B) shows that the (112) surface of Gd$_2$Te$_3$ has more positively polarized regions than negatively polarized regions. Furthermore, to confirm this, electrical conductivity calculations were performed for the chosen surface to quantify the potential of Gd$_2$Te$_3$ to generate electricity.

Utilizing the electronic structure of the system, the electronic transport properties have been calculated by solving the semi-classical Boltzmann transport equation within constant scattering time approximation (CSTA), as implemented in Boltztrap code.[45] A dense Monkhorst–Pack k-point ($21 \times 21 \times 1$) has been used for electronic transport calculations. Calculated thermopower and electrical conductivity scaled by relaxation time are shown in Figure 5C,D. At room temperature, within a carrier concentration range of 10^{12}–10^{13} cm^{-2}, a wide range of Seebeck
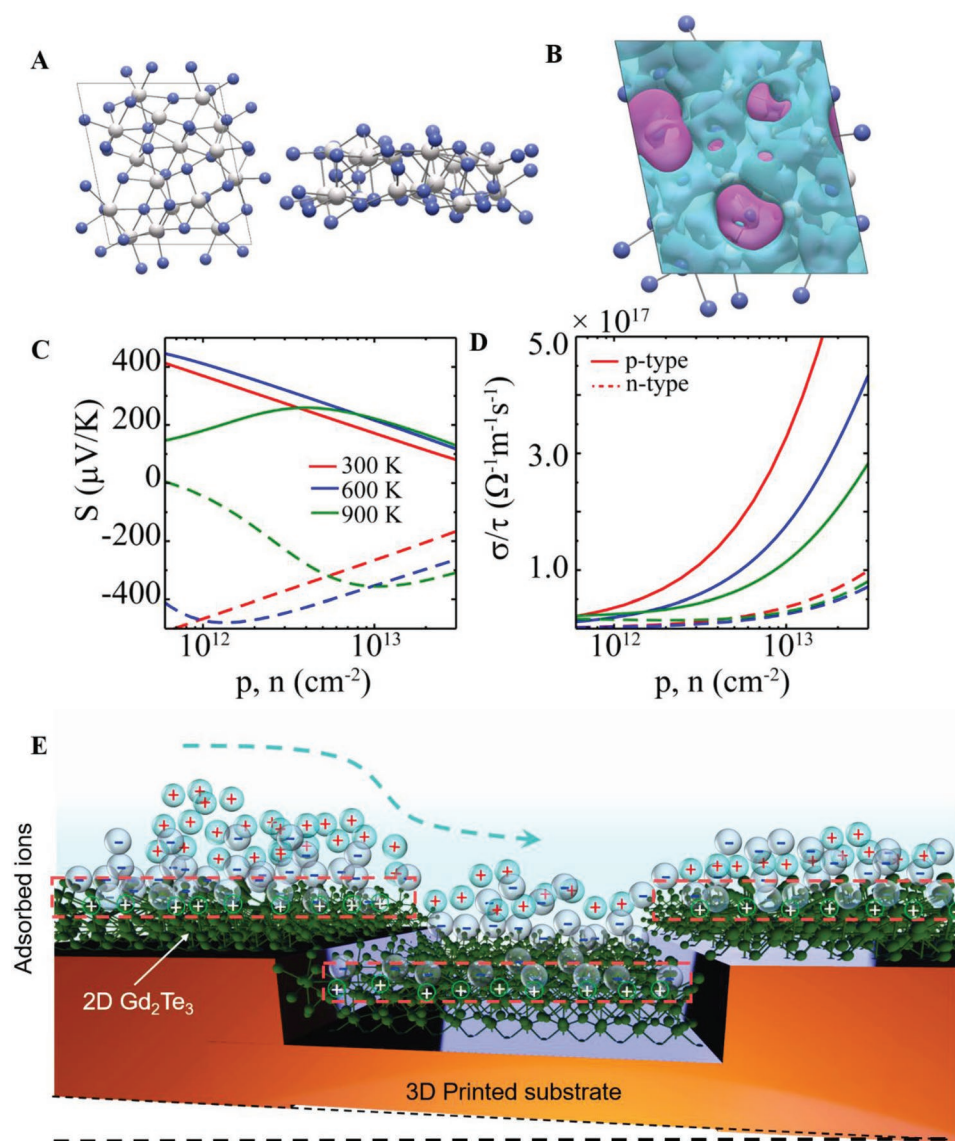
Figure 5. Electricity generation mechanism. A) (112) surface of Gd_2Te_3, on-top view, and side-on view. Grey balls represent Gd atoms and blue balls represent Te atoms. B) Charge redistribution diagram. Sky blue represents electron depleted region and pink represents the electron-accumulated region. C) Seebeck coefficient versus carrier concentration diagram and D) electronic conductivity versus carrier concentration diagram. E) Schematic diagram of charge generation mechanism due to contact electrification.

coefficient values from 300–400 µV K^{-1} have been observed for both p- and n-type charge carriers. This suggests the contribution of the charge carrier that will help generate a large amount of voltage with a given temperature gradient in this system. Additionally, in the similar carrier concentration range, at room temperature, the scaled electrical conductivity (σ/τ) exhibits a maximum of 2–4×10^{17} $\Omega^{-1}m^{-1}s^{-1}$ for p-type charge carriers. In contrast, n-type charge carriers possess a lower σ/τ. Considering the constant relaxation time approximation (CRTA), that is, with a $\tau = 10$ fs, the maximum conductivity for p-type charge carriers is 2000 S m^{-1}, which is reasonably high, implying the potential of 2D Gd_2Te_3 to generate electricity.[46] Therefore, as the electrical conductivity increases with the droplet, the attraction and release of charge play an essential role in generating electricity. Based on the theoretical calculation, the detailed

mechanism of charge transfers between the NaCl solution and Gd_2Te_3 is schematically shown in Figure 5E. As seen from the experimental results, the ions strongly affect the generation of charge in the sample. The charge concentration in the solution plays a crucial role in electrification, as we have seen in the previous result. The free ions in DI water are meager; therefore, DI droplets cannot generate much output voltage by contact electrification. However, the output voltage increases due to the electrification process after increasing free ions in the DI water by adding NaCl salt, as shown in Figure 5E. Due to the positive surface charge of the Gd_2Te_3, negatively charged Cl^- ions are attracted. As the droplet moves on the substrate, the contact area increases. The contact between the ions and Gd_2Te_3 causes more charge transfer. During the separation of droplets, the area of droplets connected to the Gd_2Te_3 gradually decreases.

From electrokinetic theory, it is known that when ionic solutions are brought in contact with solid surfaces, some of the ions adsorb onto the surface due to electrochemical interactions, forming a layer of either cations or anions depending on the surface charge of the material.[37] To balance this out, the charge accumulates on the solid surface.[8,47] Ultrathin Gd_2Te_3 has huge positive surface charges, as found from the theoretical results. Additionally, the layered nature of the 3D-printed porous structure provides sufficient surface area for the ions from the solution to adsorb. Therefore, positively charged 2D material adsorbed negative Cl^- ions on the surface and an electric double layer (EDL) is formed at the interface.[31,37] To balance this negatively charged layer of Cl^- ions, positive charges accumulate near the solid-liquid interface as the electrons move to the opposite side of the 2D material, towards the Gd_2Te_3 -polymer interface, and it suggests that charge transfer is crucial for the generation of overall output voltage (Figure 5E). The attraction and release of charge at the liquid ionic droplet play an essential role in generating electricity.

Furthermore, as mentioned earlier, the manipulation of the output performance of the device using a graphite rod can be understood as follows. Considering the different adsorption capacities of ions (Na^+, Cl^-) on Gd_2Te_3 and the graphene layer, Cl^- ions are adsorbed on Gd_2Te_3, while Na^+ ions are adsorbed on the graphene surface.[8,47] The graphene surface exchanges ions with droplets; therefore, two different charge transfer interfaces were formed, as shown by square boxes in the figure (Figure 3I).[2] Thus, the surface charge of the droplet can be manipulated by controlling the movement of the negatively charged graphene surface. As the graphite rod touches the droplet surface, the system (2D Gd_2Te_3 + droplet + graphen sheets) gives output voltage like a soft micro-robot cover upon the substrate. Therefore, contact electrification with a surface charge of the droplet can be used directly in several applications combined with lightweight, flexible 3D-printed substrates. The distribution of ions and their movement at the solid-liquid interface is a complex process, and till now, it is not fully clear. Here, we did not consider all the parameters at the molecular level of the droplet at the solid-liquid interface.

3. Conclusion

In summary, we have reported electricity generation using ultrathin 2D Gd_2Te_3 decorated 3D printed substrate as an active material. The electricity is generated directly during the movement of ionic liquid on 2D Gd_2Te_3 due to electrostatic charge transfer at the droplet boundary via contact electrification. We have also examined the output performance as a function of height, and it shows a linear increment with height. More importantly, the energy harvesting capability of Gd2Te3 decorated porous objects is further successfully enhanced with random porosity structures. The DFT calculations confirm the presence of predominant positive polarity over the surface of Gd_2Te_3 that interacts with a solution to generate electricity with a wide range of Seebeck coefficients. This is further supported by the calculated high electrical conductivity of $2–4 \times 10^{17} \ \Omega^{-1} m^{-1} s^{-1}$ for p-type charge carriers. Additionally, the output voltage was manipulated using a graphite rod by charge accumulations. Therefore, coupling ultrathin 2D materials and 3D printing technology can be a good choice for various applications in energy harvesting, biomedical sectors, sensors, hydrodynamic sensors, etc.

4. Experimental Section

Materials: Bulk Gd_2Te_3 was fabricated using the vacuum induction melting method. Metal samples of 99.99% purity of Gd and Te were used for preparing the compound containing 4.7 g of Gd and 5.3 g of Te. The alloys were prepared by melting the constituent element at a temperature of 1250 °C in a quartz tube using vacuum induction melting in an argon atmosphere and allowed to cool naturally in Ar. 2D sheets of Gd_2Te_3 were synthesized using ultrasonication-assisted liquid phase exfoliation with 2-propanal (IPA) as solvent. 1.5 g of powdered Gd_2Te_3 was ultrasonicated at 30 kHz in 300 mL of IPA for 30 min. Using 2-Propanol (isopropyl alcohol or IPA) for exfoliation was primarily driven by its low toxicity compared to other solvents and its high volatility, which allows depositing 2D sheets on surfaces.

Preparation of Porous 3D Printed Structure: The $15 \times 30 \times 0.08$ mm ($L \times B \times H$) specification of the structures were fabricated using polylactic acid filament of 1.75 mm (with tolerance ± 0.1 mm) diameter via extrusion-based Flashforge adventure 3 printers. The triangular porous structure has a triangular prism pore (base side-1.01 mm and height-0.08 mm), the hexagonal porous structure has a right regular hexagonal prism pore (base edge- 0.595 mm and height- 0.08 mm), and the random porous structure has pore diameter ranges from 0.5 to 1.2 mm. The porous structures were printed at an extruder temperature of 210 °C and platform temperature of 50 °C with a print speed of 40 mm s^{-1} and travel speed of 70 mm s^{-1}. The infill density was kept at 60% for hexagonal, triangular, and line porosity whereas for random porosity it was kept at 100%. All the structures are printed at hyper resolution (single layer thickness of 80 µm) and the solidification of post-printed structures was carried out with the help of forced fan cooling.

Characterizations: X-ray diffraction (XRD) patterns of the crystalline phases of the drop-casted 2D Gd_2Te_3 were obtained by X-ray diffractometer (Bruker, D8 Advance) with a Cu-Kα ($\lambda = 1.5406$Å) radiation source, operating at 40 kV voltage and 40 mA current. Scanning electron microscopy (SEM-Jeol JSM-IT300HR) operated at an acceleration voltage of 20 kV and 7.475 nA was used to image both bulk and 2D Gd_2Te_3. Transmission electron microscopy (TEM-JEM 2100 HRTEM) and Atomic force microscope (AFM, Nanosurf easy scan 2) was used to image the 2D sheets. Attached energy dispersion spectrometer units to both SEM and TEM were used to get a composition of both bulk and 2D Gd_2Te_3. The particle size distribution and zeta potential were obtained from Horiba Scientifica Nano Particle Analyzer SZ-100. Raman spectroscopy was done using WITec UHTS Rama Spectrometer (WITec, UHTS 300 VIS, Germany) at the laser excitation wavelength of 532 nm at Room Temperature (RT). The optical absorbance property of pristine 2D Gd_2Te_3 was characterized using a UV–vis spectrometer from 200 to 800 nm. The output voltage of the hybrid nanogenerator was measured by a digital storage oscilloscope (DSO, Tektronix, TBS1072B).

Computational Methodology: DFT was done with the Vienna ab initio simulations (VASP) package.[48] The electron-ion interactions were described using the all-electron projector augmented wave pseudopotentials,[49] and Perdew–Bruke–Ernzehof (PBE) generalized gradient approximation (GGA)[50] was used to approximate the electronic exchange correlations with an effective on-site Hubbard (U_{eff} = U–J = 6 eV) parameter was used for the Gd- states in DFT+U method as introduced by Dudarev et al.[51] The plane-wave kinetic energy cut-off of 520 eV was used. All the structures were optimized using a conjugate gradient scheme until the energies and the components of forces reached 10^{-6} eV and 0.001 eV Å^{-1} for bulk Gd_2Te_3 and 10^{-5} and 0.01 eV Å^{-1} for (112) surface of Gd_2Te_3, respectively. A vacuum of 10 Å was added in the z-direction to prevent interactions between the periodic images. The Brillouin zone of bulk Gd_2Te_3 and (112) surface of Gd_2Te_3 were sampled with $7 \times 7 \times 7$ and $3 \times 3 \times 1$ Monkhorst–Pack, respectively. All the calculations were spin-polarized.

Supporting Information

Acknowledgements

Conflict of Interest

The authors declare no conflict of interest.

Data Availability Statement

The data that support the findings of this study are available from the corresponding author upon reasonable request.

Keywords

[1] S. Chu, A. Majumdar, *Nature* **2012**, *488*, 294.

[2] J. Xiong, M. F. Lin, J. Wang, S. L. Gaw, K. Parida, P. S. Lee, *Adv. Energy Mater.* **2017**, *7*, 1701243.

[3] J. Nie, Z. Ren, L. Xu, S. Lin, F. Zhan, X. Chen, Z. L. Wang, *Adv. Mater.* **2020**, *32*, 1905696.

[4] S. Nie, H. Guo, Y. Lu, J. Zhuo, J. Mo, Z. L. Wang, *Adv. Mater. Technol.* **2020**, 2000454.

[5] J. Nie, Z. Wang, Z. Ren, S. Li, X. Chen, Z. L. Wang, *Nat. Commun.* **2019**, *10*, 2264.

[6] L. Zhao, L. Liu, X. Yang, H. Hong, Q. Yang, J. Wang, Q. Tang, *J. Mater. Chem. A* **2020**, *8*, 7880.

[7] Z. L. Wang, T. Jiang, L. Xu, *Nano Energy* **2017**, *39*, 9.

[8] J. Yin, X. Li, J. Yu, Z. Zhang, J. Zhou, W. Guo, *Nat. Nanotechnol.* **2014**, *9*, 378.

[9] N. Li, C. Yu, Z. Dong, L. Jiang, *Soft Matter* **2020**, *16*, 9176.

[10] F. Mugele, J.-C. Baret, *J. Phys.: Condens. Matter* **2005**, *17*, R705.

[11] J. A. Lv, Y. Liu, J. Wei, E. Chen, L. Qin, Y. Yu, *Nature* **2016**, *537*, 179.

[12] C. Zhu, T. Liu, F. Qian, T. Y. J. Han, E. B. Duoss, J. D. Kuntz, C. M. Spadaccini, M. A. Worsley, Y. Li, *Nano Lett.* **2016**, *16*, 3448.

[13] K. Ghosh, M. Pumera, *Nanoscale* **2021**, *13*, 5744.

[14] Z. Tian, X. Tong, G. Sheng, Y. Shao, L. Yu, V. Tung, J. Sun, R. B. Kaner, Z. Liu, *Nat. Commun.* **2019**, *10*, 4913.

[15] L. Yu, Z. Fan, Y. Shao, Z. Tian, J. Sun, Z. Liu, *Adv. Energy Mater.* **2019**, *9*, 1901839.

[16] R. S. Ambekar, B. Kushwaha, P. Sharma, F. Bosia, M. Fraldi, N. M. Pugno, C. S. Tiwary, *Mater. Today* **2021**, *48*, 72.

[17] E. García-Tón, S. Barg, J. Franco, R. Bell, S. Eslava, E. D'Elia, R. C. Maher, F. Guitian, E. Saiz, *Adv. Mater.* **2015**, *27*, 1688.

[18] R. S. Ambekar, E. F. Oliveira, B. Kushwaha, V. Pal, P. M. Ajayan, A. K. Roy, D. S. Galvao, C. S. Tiwary, *Addit. Manuf.* **2021**, *47*, 102297.

[19] B. Kushwaha, K. Dwivedi, R. S. Ambekar, V. Pal, D. P. Jena, D. R. Mahapatra, C. S. Tiwary, *Adv. Eng. Mater.* **2021**, *23*, 2001471.

[20] R. S. Ambekar, I. Mohanty, S. Kishore, R. Das, V. Pal, B. Kushwaha, A. K. Roy, S. Kumar Kar, C. S. Tiwary, *Adv. Eng. Mater.* **2021**, *23*, 2001428.

[21] B. Chen, W. Tang, Z. L. Wang, *Mater. Today* **2021**, *50*, 224.

[22] M. Yuan, C. Li, H. Liu, Q. Xu, Y. Xie, *Nano Energy* **2021**, *85*, 105962.

[23] C. Shao, Y. Zhao, L. Qu, *SusMat* **2022**, *2*, 142.

[24] H. Li, R. Li, X. Fang, H. Jiang, X. Ding, B. Tang, G. Zhou, R. Zhou, Y. Tang, *Nano Energy* **2019**, *58*, 447.

[25] J. Zhao, Q. Deng, T. H. Ly, G. H. Han, G. Sandeep, M. H. Rümmeli, *Nat. Commun.* **2015**, *6*, 8935.

[26] L. M. Schoop, M. N. Ali, C. Straßer, A. Topp, A. Varykhalov, D. Marchenko, V. Duppel, S. S. P. Parkin, B. V. Lotsch, C. R. Ast, *Nat. Commun.* **2016**, *7*, 11696.

[27] D. A. Zocco, J. J. Hamlin, K. Grube, J. H. Chu, H. H. Kuo, I. R. Fisher, M. B. Maple, *Phys. Rev. B: Condens. Matter Mater. Phys.* **2015**, *91*, 205114.

[28] S. Siddique, C. Chowde Gowda, S. Demiss, R. Tromer, S. Paul, K. K. Sadasivuni, E. F. Olu, A. Chandra, V. Kochat, D. S. Galvão, P. Kumbhakar, R. Mishra, P. M. Ajayan, C. Sekhar Tiwary, *Mater. Today* **2021**, *51*, 402.

[29] S. Siddique, C. C. Gowda, R. Tromer, S. Demiss, A. R. S. Gautam, O. E. Femi, P. Kumbhakar, D. S. Galvao, A. Chandra, C. S. Tiwary, *ACS Appl. Nano Mater.* **2021**, *4*, 4829.

[30] S. D. Negedu, R. Tromer, C. C. Gowda, C. F. Woellner, F. E. Olu, A. K. Roy, P. Pandey, D. S. Galvao, P. M. Ajayan, P. Kumbhakar, C. S. Tiwary, *Nanoscale* **2022**, *14*, 7788.

[31] A. S. Aji, R. Nishi, H. Ago, Y. Ohno, *Nano Energy* **2020**, *68*, 104370.

[32] J. S. Swinnea, H. Steinfink, L. R. Danielson, *J. Appl. Crystallogr.* **1987**, *20*, 102.

[33] I. P. Muthuselvam, R. Nehru, K. R. Babu, K. Saranya, S. N. Kaul, S. M. Chen, W. T. Chen, Y. Liu, G. Y. Guo, F. Xiu, R. Sankar, *J. Phys.: Condens. Matter* **2019**, *31*, 285802.

[34] P. Arun, A. G. Vedeshwar, *J. Mater. Sci.* **1996**, *31*, 6507.

[35] C. F. Holder, R. E. Schaak, *ACS Nano* **2019**, *13*, 7359.

[36] S. Lei, J. Lin, Y. Jia, M. Gray, A. Topp, G. Farahi, S. Klemenz, T. Gao, F. Rodolakis, J. L. McChesney, C. R. Ast, A. Yazdani, K. S. Burch, S. Wu, N. P. Ong, L. M. Schoop, *Sci. Adv.* **2020**, *6*, aay6407.

[37] J. Dong, F. R. Fan, Z.-Q. Tian, *Nanoscale* **2021**, *13*, 17290.

[38] Y. Zhang, Q. Tang, B. He, P. Yang, *J. Mater. Chem. A* **2016**, *4*, 13235.

[39] D. Park, S. Won, K.-S. Kim, J.-Y. Jung, J.-Y. Choi, J. Nah, *Nano Energy* **2018**, *54*, 66.

[40] H. Li, D. Zhang, H. Wang, Z. Chen, N. Ou, P. Wang, D. Wang, X. Wang, J. Yang, *Small* **2018**, *15*, 1804146.

[41] S. Ho Lee, D. Kim, S. Kim, C.-S. Han, *Appl. Phys. Lett.* **2011**, *99*, 104103.

[42] H. Zhong, J. Xia, F. Wang, H. Chen, H. Wu, S. Lin, *Adv. Funct. Mater.* **2017**, *27*, 1604226.

[43] Z. Ge, Y. Wang, *J. Phys. Chem. B* **2017**, *121*, 3394.

[44] A. Jain, S. P. Ong, G. Hautier, W. Chen, W. D. Richards, S. Dacek, S. Cholia, D. Gunter, D. Skinner, G. Ceder, K. A. Persson, *APL Mater.* **2013**, *1*, 011002.

[45] G. K. H. Madsen, D. J. Singh, *Comput. Phys. Commun.* **2006**, *175*, 67.

[46] D. Sheberla, L. Sun, M. A. Blood-Forsythe, S. Er, C. R. Wade, C. K. Brozek, A. Aspuru-Guzik, M. Dincă, *J. Am. Chem. Soc.* **2014**, *136*, 8859.

[47] S. S. Kwak, S. Lin, J. H. Lee, H. Ryu, T. Y. Kim, H. Zhong, H. Chen, S. W. Kim, *ACS Nano* **2016**, *10*, 7297.

[48] G. Kresse, J. Hafner, *Phys. Rev. B* **1993**, *47*, 558.

[49] G. Kresse, D. Joubert, *Phys. Rev. B* **1999**, *59*, 1758.

[50] J. P. Perdew, K. Burke, M. Ernzerhof, *Phys. Rev. Lett.* **1996**, *77*, 3865.

[51] S. L. Dudarev, G. A. Botton, S. Y. Savrasov, C. J. Humphreys, A. P. Sutton, *Phys. Rev. B* **1998**, *57*, 1505.

ADVANCED
SUSTAINABLE
SYSTEMS

Supporting Information

Rain Energy Harvesting Using Atomically Thin Gadolinium Telluride Decorated 3D Printed Nanogenerator

Partha Kumbhakar, Arko Parui, Rushikesh S. Ambekar, Madhubanti Mukherjee, Saif Siddique, Nicola M. Pugno, Abhishek K. Singh, and Chandra S. Tiwary*

Supplementary Materials

Rain energy harvesting using atomically thin Gadolinium Telluride decorated 3D Printed nanogenerator

Partha Kumbhakar[§], Arko Parui[§], Rushikesh S. Ambekar, Madhubanti Mukherjee, Saif Siddique, Nicola M. Pugno*, Abhisek K. Singh*, Chandra S. Tiwary*

§-Equal contribution

Dr. Partha Kumbhakar, Mr. Rushikesh S. Ambekar, Mr. Saif Siddique, Prof. C. S. Tiwary, Department of Metallurgical and Materials Engineering, Indian Institute of Technology Kharagpur, West Bengal, 721302 India
Email: chandra.tiwary@metal.iitkgp.ac.in

Mr. Arko Parui, Ms. Madhubanti Mukherjee, Prof. Abhisek K. Singh
Indian Institute of Science, Bangalore 560012, India
Email: abhishek@iisc.ac.in,

Prof. Nicola M. Pugno
Laboratory of Bio-inspired, Bionic, Nano, Meta Materials and Mechanics, Department of Civil, Environmental and Mechanical Engineering, University of Trento, Italy

School of Engineering and Materials Science, Queen Mary University of London, Mile End Road, London E1 4NS, UK

Email: nicola.pugno@unitn.it

This PDF file includes:

> Figs. S1 to S8
> Captions for Data S1 to S8
> Supplementary Movie S1 and S2
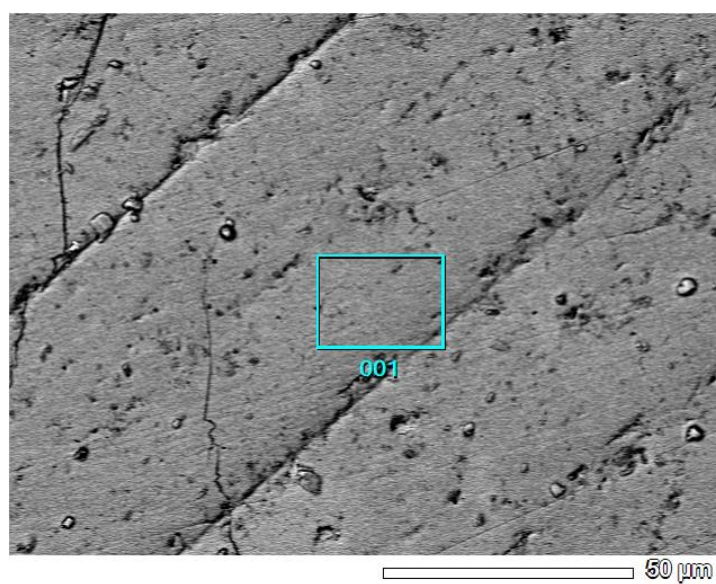
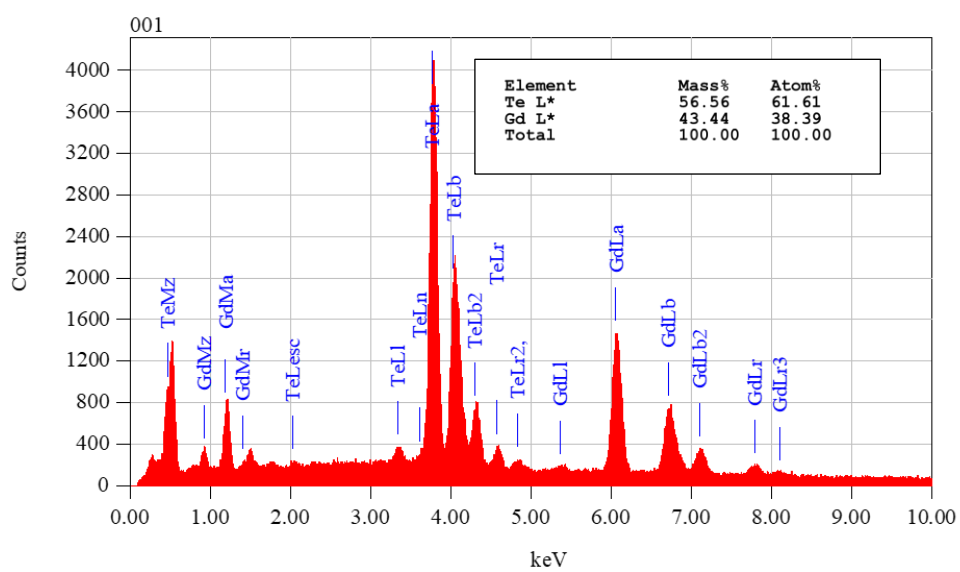**Figure S1**. SEM image of bulk Gd_2Te_3

Figure S2: EDX spectra of bulk sample. Inset shows the elemental compositions.
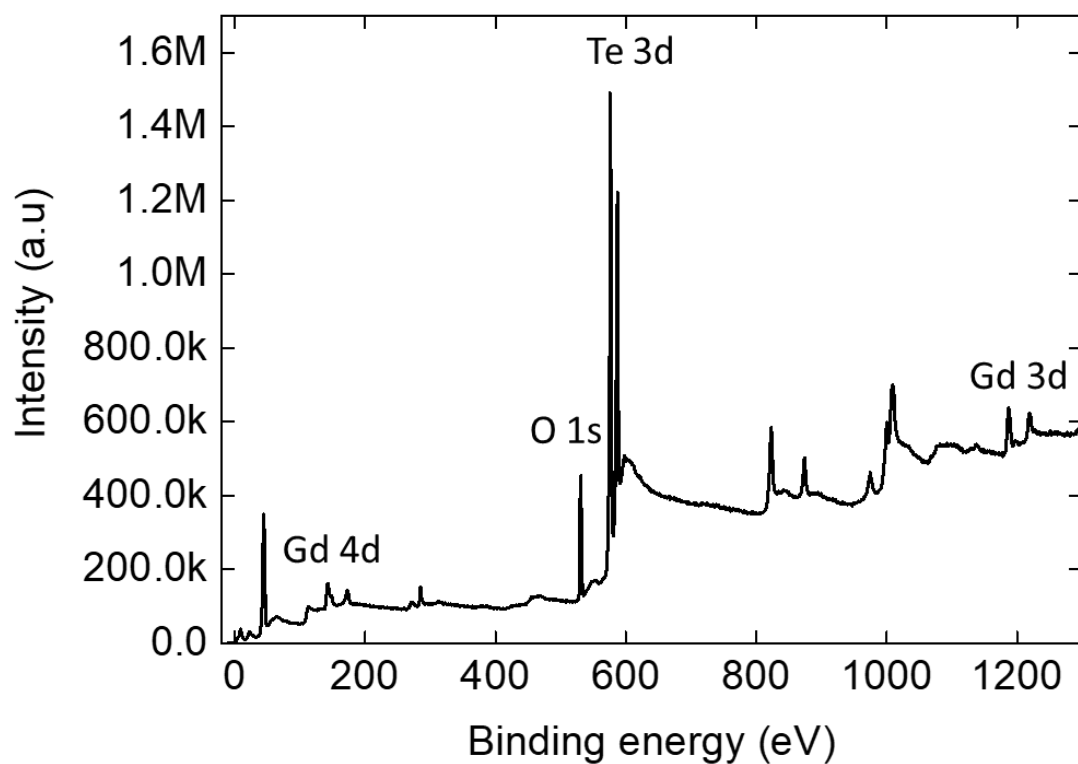
Figure S3. Full scan XPS spectrum of exfoliated Gd_2Te_3
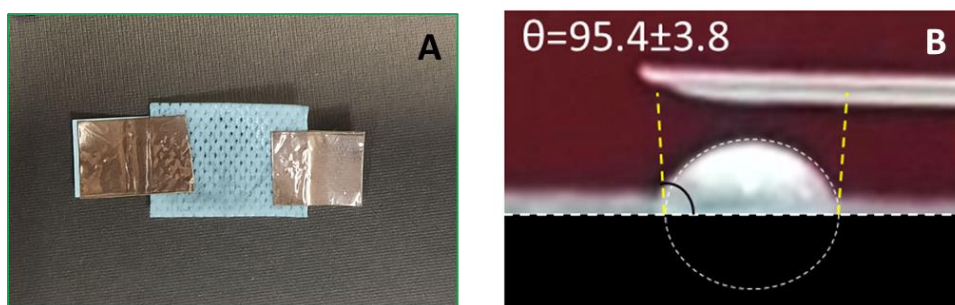

Figure S4. (A) Digital photograph of the coated 3D printed cell. **(B)** Contact angle on the surface of the cell.
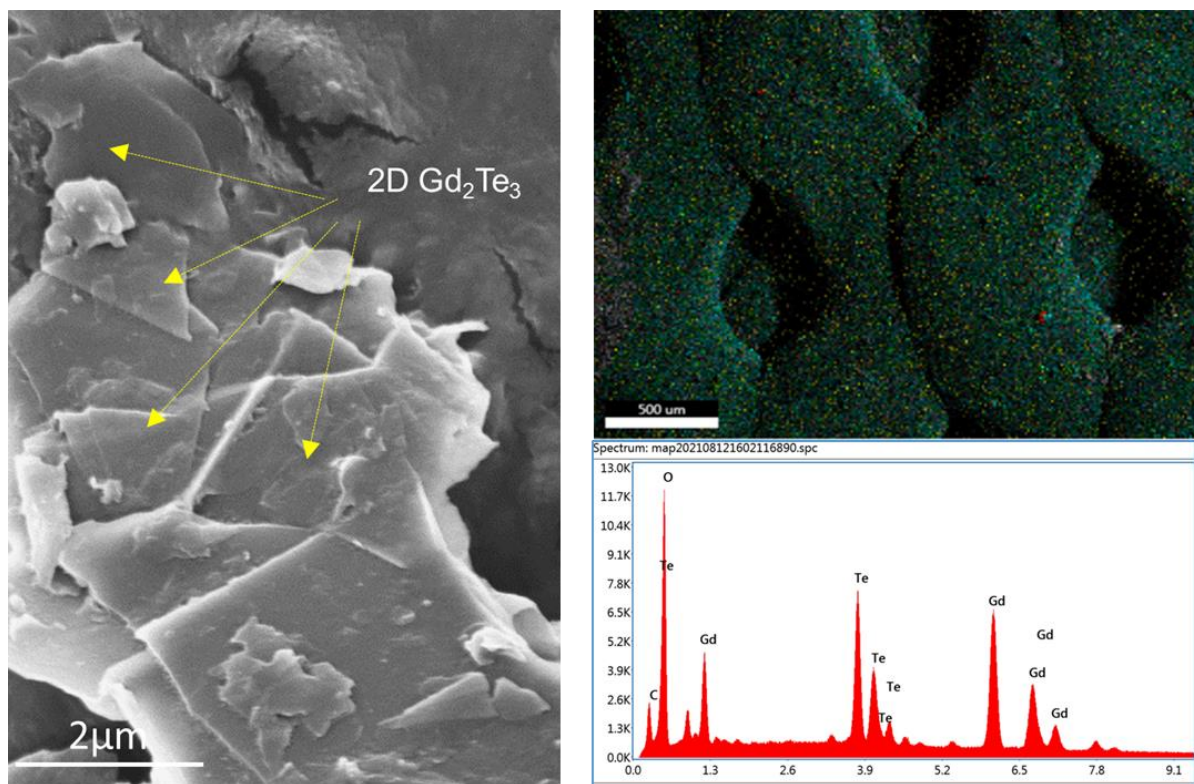
Figure S5: SEM image, Elemental mapping and EDX spectra of 3D printing object after
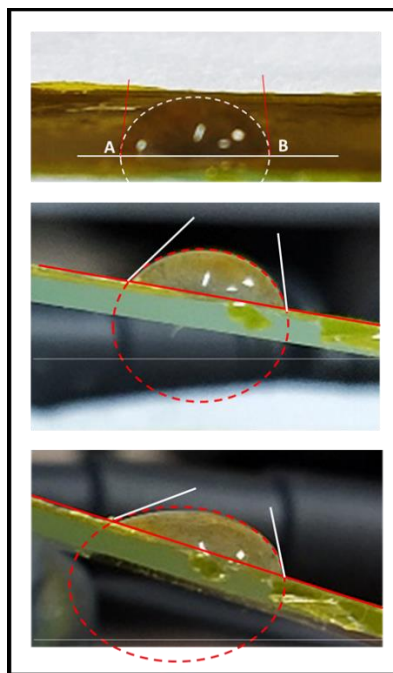
coating with exfoliated sample.

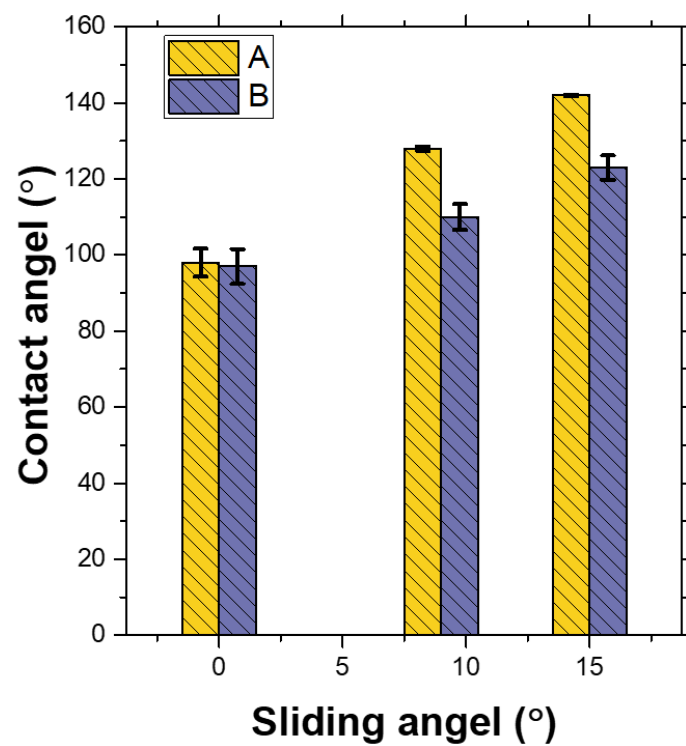**Figure S6:** Digital photographs of the droplet as function of sliding angle

Figure S7: Increase of contact angle as a function of sliding angle. A and B is described in
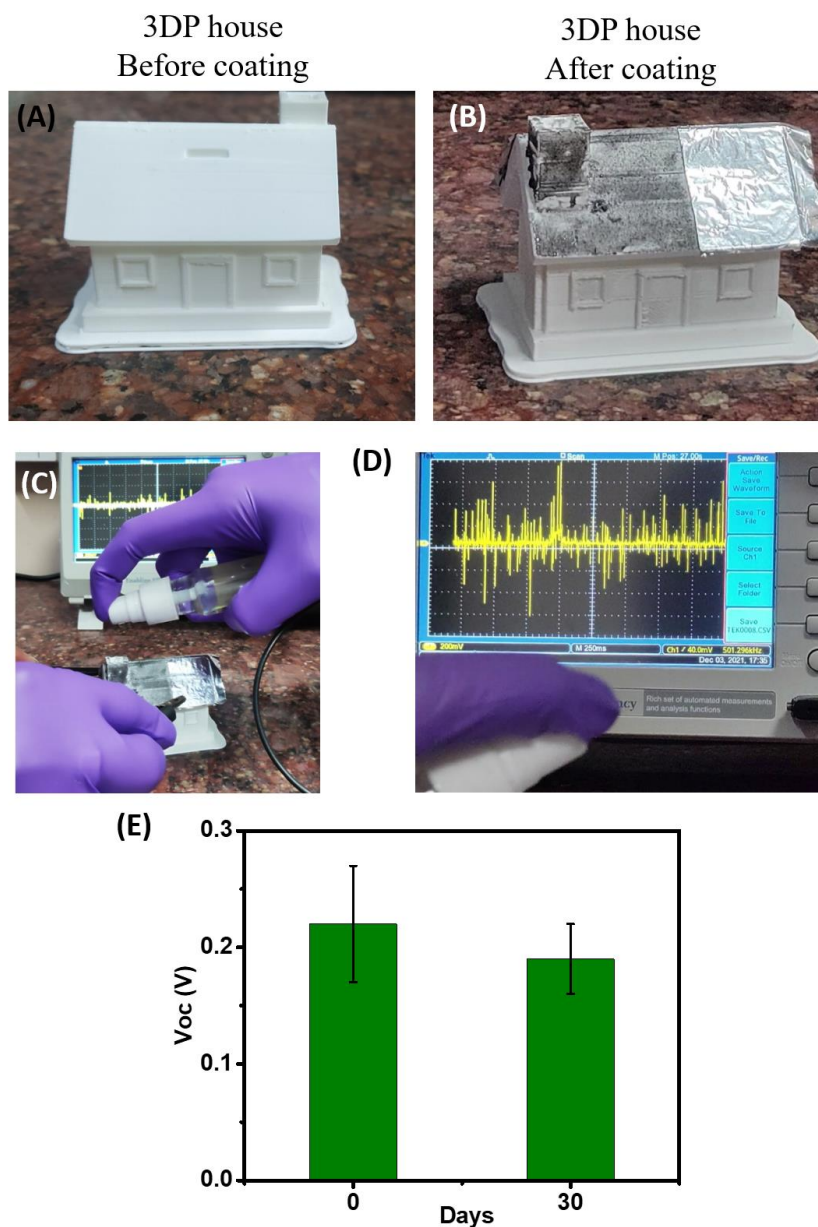
the upper panel of Figure S6.

Figure S8: 3DP smart house (A) before and (B) after coating with exfoliated Gd$_2$Te$_3$. (C) and (D) Snapshots of the output voltage in presence of artificial raindrops. (E) Stability test of the 3DP house after 30 days.
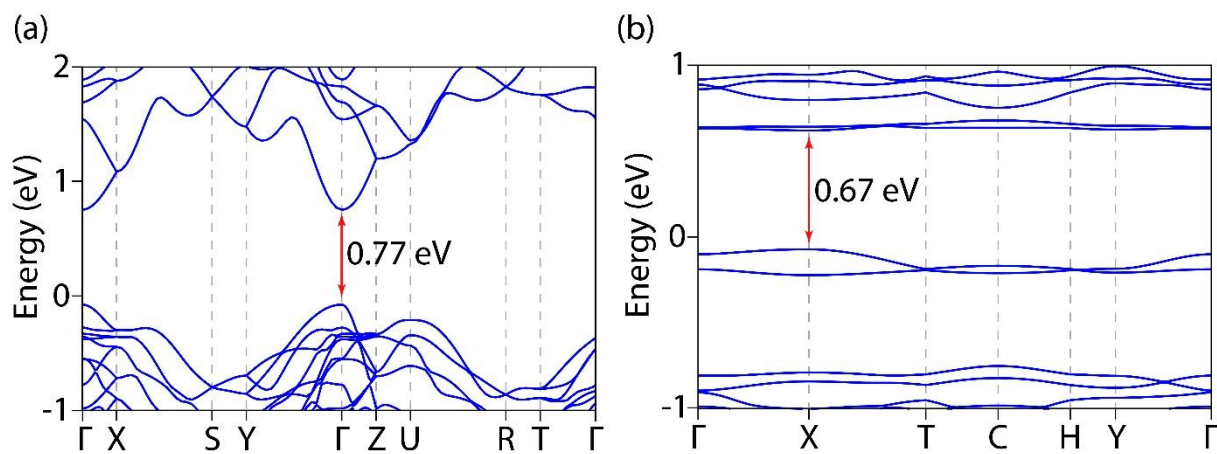
Figure S9: Band structure diagram of (a) bulk Gd_2Te_3 and (b) (112)-Gd_2Te_3 surface.

Movie S1: Output voltage as a function of multiple droplet falling.

Movie S2: Output voltage from 3DP smart house in presence of artificial raindrops